Zeppilli, D., Pouya, A., Zhu, C. *et al.* Numerical analysis of injection-induced fault reactivation using hydro-mechanical coupled finite element model with cohesive zone elements. *Geomech. Geophys. Geo-energ. Geo-resour.* 7, 62 (2021). https://doi.org/10.1007/s40948-021-00259-0

Numerical Analysis of Injection-induced Fault Reactivation Using Hydro-Mechanical Coupled Finite Element Model with Cohesive Zone Elements

Danilo Zeppilli[1,2], Amade Pouya[3], Cheng Zhu[1,2], Xiang-Chao Shi[1], Hao Xu[4]

[1]State Key Laboratory of Oil and Gas Reservoir Geology and Exploitation, Southwest Petroleum University

[2]Department of Civil and Environmental Engineering, Rowan University

[3]Laboratoire Navier (UGE-ENPC-CNRS), Université Gustave Eiffel, France

[4]Energy Geosciences Division, Lawrence Berkeley National Laboratory

Corresponding author: Cheng Zhu (zhuc@rowan.edu)

Highlights:

- Hydro-mechanical model simulates pore pressure perturbation under varying injection duration, injection rate, and formation permeability.
- Progressive damage in cohesive zone elements reflects the effects of stress redistribution on fault reactivation and slip.
- The triggering of fault instability in Timpson is associated with sudden damage propagation and stress relaxations.

Abstract

Fault instability in response to subsurface wastewater injection is controlled by various operation- and site-dependent parameters. Previous numerical approaches focus on the prediction of the onset of fault reactivation, whereas the subsequent stress redistribution and fault movement are not considered. To better understand the potential correlation between injection activities and fault instability, we develop a hydro-mechanical coupled finite element model and use the May 2012 Timpson earthquake sequence as a case study. Cohesive zone model integrating hyperbolic damage criterion and weakening behaviors is assigned to element interface to represent the nearby fault and capture the resulting fault behaviors under fluid injection. Simulation results indicate that this model is able to reveal the spatiotemporal evolution of pore pressure and geomechanical stress field at the Timpson site. Under continual fluid injection, pore pressure increases and gradually stabilizes, more evident in regions close to the injection layer. Poroelastic stress and pore pressure changes jointly influence the fault stability. Through damage evolution considered in the cohesive zone model, the finite element model can simulate the foreshock and main shock of the Timpson earthquake sequence, associated with fault displacement and stress relaxation. Once the damage criterion is reached, the stress redistribution at the failed fault segment induces further increase of stress on the other domains of the fault, which drives subsequent fault slip. This study brings new insights into the numerical modeling of induced earthquakes and highlights the importance of accounting for fluid injection activities to minimize the potential of fault reactivation and slip.

Keywords: induced earthquake, cohesive zone model, hydro-mechanical coupling, fault reactivation and slip, finite element model

1. Introduction

In the energy industry, oil and gas extraction and hydraulic fracture stimulation of unconventional reservoirs typically result in significant amounts of underground formation water. Injection of wastewater into sedimentary reservoirs overlying the crystalline basement is a common method of wastewater disposal, which has been known to induce earthquakes from the 1960s (Healy et al. 1968; Hsieh and Bredehoeft 1981). However, due to their higher magnitudes and more frequent occurrence, similar induced earthquakes have not been well documented until recently. In the eastern and central United States, a sharp increase in the number of injection-induced earthquakes, especially those with magnitudes greater than 3, has been observed since 2009(Ellsworth 2013; Horton 2012; Keranen et al. 2014; McGarr et al. 2015; Rubinstein and Mahani 2015; Walsh III and Zoback 2016; Weingarten et al. 2015). The increasing number of earthquake events in areas with active fluid injection but low natural seismicity has attracted the interests of numerous researchers in the coupled phenomena of fluid migration, poroelastic stress changes, and induced seismicity (Da Silva and Einstein 2013; Ellsworth 2013; Fan et al. 2016; McGarr et al. 2015; Rutqvist et al. 2013; Segall and Lu 2015; Zhu et al. 2017).

The potential of fault reactivation in response to subsurface fluid injection is governed by the interplay of natural factors (e.g., fault geometry, fault orientation and distribution, in-situ stress state, initial pore fluid pressure, and reservoir permeability) and anthropogenic factors (e.g., injection rate, cumulative injected volume, wellhead injection pressure, production rate, and distance of injectors from the mapped faults) (Fan et al. 2016; Gunarathna and da Silva 2019; Haddad and Eichhubl 2020; Hornbach et al. 2015; Kang et al. 2019; McGarr 2014; Segall and Lu 2015; Weingarten et al. 2015). It becomes more important to understand the dependence of fault reactivation on various factors and to minimize fluid injection-induced potential hazards. Among

injection wells across four central states in the U.S. including Oklahoma, Arkansas, Colorado, and New Mexico, the maximum monthly injection rate differs by several orders of magnitude from 15.9 m^3/month up to 318,000 m^3/month (Weingarten et al. 2015). Three seismic sequences that have occurred in Texas, including the 2008-2013 Dallas-Fort Worth Airport sequence (Frohlich et al. 2011), the 2012 Timpson sequence (Frohlich et al. 2014), and the 2013 Azle sequence (Hornbach et al. 2015), are all located within about 2 km of active injection wells with 24,000 m^3 or higher monthly injection rate (Frohlich et al. 2016). Fluid injection rates can differ dramatically over time or at different locations (Frohlich et al. 2014; Keranen et al. 2014). The excess pressure above the background pore fluid pressure generated by these fluid injection activities decreases the effective normal stress on the fault and potentially leads to fault reactivation (Block et al. 2014; Kim 2013; Yeo et al. 2020). The correlation between the timing of fluid injection and seismicity remains complicated and depends on both natural and anthropogenic factors (Frohlich 2012; Hornbach et al. 2015).

A number of theoretical studies have been conducted within the rigorous framework of Biot poroelasticity to investigate the coupled effects of pore pressure and stress changes due to fluid injection. An analytical solution has been derived for stress and pore pressure in an infinite homogeneous poroelastic domain subjected to a continuous point source (Rudnicki 1986). The solution for a fluid line source for a plane strain case was also obtained using a superposition approach. Detournay and Cheng (1987) presented the fundamental solution for a two-dimensional plane strain continuous fluid source case. Rajapakse and Senjuntichai (1993) acquired the fundamental solutions for a poroelastic half space with compressible constituents under an arbitrary ring fluid source. Cheng and Detournay (1998) derived the closed-form fundamental solutions for instantaneous and continuous fluid source in three dimensional homogenous

poroelasticity. Chen (2003) presented the semi-analytical solution for fluid injection into a multi-layered poroelastic half-space with incompressible solid grains. Selvadurai and Kim (2015) gave the analytical solution for displacement and pore pressure associated with extraction of fluids from a poroelastic half-space. Although it is desirable to seek analytical or semi-analytical solutions for fluid injection into a layered poroelastic medium transected by heterogeneous faults, to the best of our knowledge, no analytical solution is available for a heterogeneous geologic profile containing layered strata and inclined faults. To simulate the effect of multi-physics coupled fluid injection processes on the stability of fault structure, numerical methods were used. Finite element models have been set up to simulate the reactivation of faults that extend through the basement (Chang and Segall 2016; Fan et al. 2016; Fan et al. 2019; Johann et al. 2018; Lei et al. 2021; Rutqvist et al. 2013; Zhu et al. 2017). The simplified Coulomb failure criterion governs fault reactivation in these models, which necessitates the post-analysis of simulated stress state and pore pressure results to determine the onset of fault reactivation. Barbour et al. (2017) used the spectral element method of Wang and Kümpel (2003) to calculate time-varying cylindrically symmetric solutions in a layered half space, with fault not explicitly included in the model. In earthquake fracture mechanics, both the rupture front propagation and the evolution of friction on the remainder of the slipping surface should be considered. Most existing numerical approaches, however, do not account for the coupling of crack propagation and friction evolution, which is critical to modeling the transient process and fault slip instabilities. Unstable fault movement generates a seismic signal, which is distinguished by a brutal propagation of damage along the fault and a sudden elastic energy drop. It is critical to consider the fault slip process in order to advance our understanding of the relationship between fluid injection and induced earthquakes.

To simulate the effects of fluid injection activities on fault instability, a hydro-mechanical fully coupled finite element model was applied in this study. Cohesive zone elements were used to assess the onset of fault reactivation and the subsequent fault slip resulting from geomechanical stress changes and pore pressure perturbations. We used the model to assess the potential correlation between the volume and rate of fluid injected into disposal wells and seismic fault slip on nearby faults during the 4.8M_W 2012 Timpson seismic event in east Texas. The model estimated the normal and shear stress changes in the reservoir layer as well as fault displacements under fluid injection. Although adopting a similar model geometry as the one developed in (Fan et al. 2016), the model developed in this study is fundamentally different from the work in (Fan et al. 2016). Their model belongs to a poroelasticity model, which simulates the stress state change in the continuum domain assuming that the material remains elastic. Fault reactivation is determined through the Coulomb's criterion by the post-processing of the simulation results using the poroelastic stress and pore pressure as input. Their model only simulates the stress change and pore pressure perturbation before fault reactivation, and cannot be used to predict stress state update after fault reactivation or any subsequent fault slip processes. In comparison, this study uses a damage cohesive zone model that includes not only continuum bulk elements but also joint elements. The model considers poroelasticity, as well as damage evolution along the fault discontinuity. Fault reactivation is considered simultaneously in the simulation through the damage initiation and accumulation in the cohesive zone elements. The model enables capturing not only fault reactivation, but also post-slip induced stress relaxation and pore pressure perturbation.

136 The following is the structure of the paper. Section 2 summarizes the Timpson site's geological
137 conditions, 2012 May earthquake information, and injection time history. Section 3 describes
138 various injection scenarios as well as the configuration of the finite element model enriched with
139 cohesive zone elements. Section 4 shows the temporal and spatial variations in pore pressure, stress
140 field, and fault displacement under various injection scenarios.

141

142 2. Site Condition

143 Timpson is a city located in the eastern part of Texas. On 17 May 2012, a Mw 4.8 earthquake
144 occurred, causing significant tremor to local residents and certain damage to ground buildings.
145 Prior to this event, seismicity was uncommon in this area, with the most recent earthquake
146 occurring in 1981 (Frohlich and Davis 2002). Based on the felt reports from this May 2012
147 Earthquake and the records of regional seismic stations, it has been learned that a number of
148 foreshocks occurred before the main shock. The nearest permanent seismic station is the U.S.
149 National Network Station NATX in Nacogdoches, which is situated approximately 25 km
150 southwest of the highest-intensity region and starts its operation since 2004. Approximately 18
151 months after the onset of injection in 2006, the earliest event occurred in April 2008, with a
152 relatively small magnitude and not felt by local residents. 69 months after wastewater injection,
153 the Mw4.8 earthquake occurred, following a sequence of smaller earthquakes. According to the
154 analysis of field data, epicenters are located near a mapped basement fault and near high-volume
155 injection wells (Fig. 1), with focal depths in the range of 1.7-4.5 km identified to be at or below
156 the depths of injection (Fan et al. 2016; Frohlich et al. 2014). The deployment of more temporary
157 seismic stations in February 2013 helped locate aftershocks that aligned along a mapped fault

striking about N42°W (Jackson 1982). Borehole breakouts and induced fractures in the nearby injection well, together with the focal mechanism of the Mw4.8 event, indicate a normal/strike-slip faulting stress regime. Note that exact earthquake locations, fault plane geometry, and in-situ stress and pore pressure conditions may vary depending on more recent works (Shirzaei et al. 2016; Shirzaei et al. 2019; Snee 2020; Snee and Zoback 2020; Wang et al. 2020; Zhai and Shirzaei 2018). As the primary goal of this study is to demonstrate the possible application of a cohesive zone model for fault reactivation and slip predictions, we configured the model using the prior work by (Fan et al. 2016) as a basis. Future investigations will take into account of all these recent findings, as well as any possible future update on site conditions.

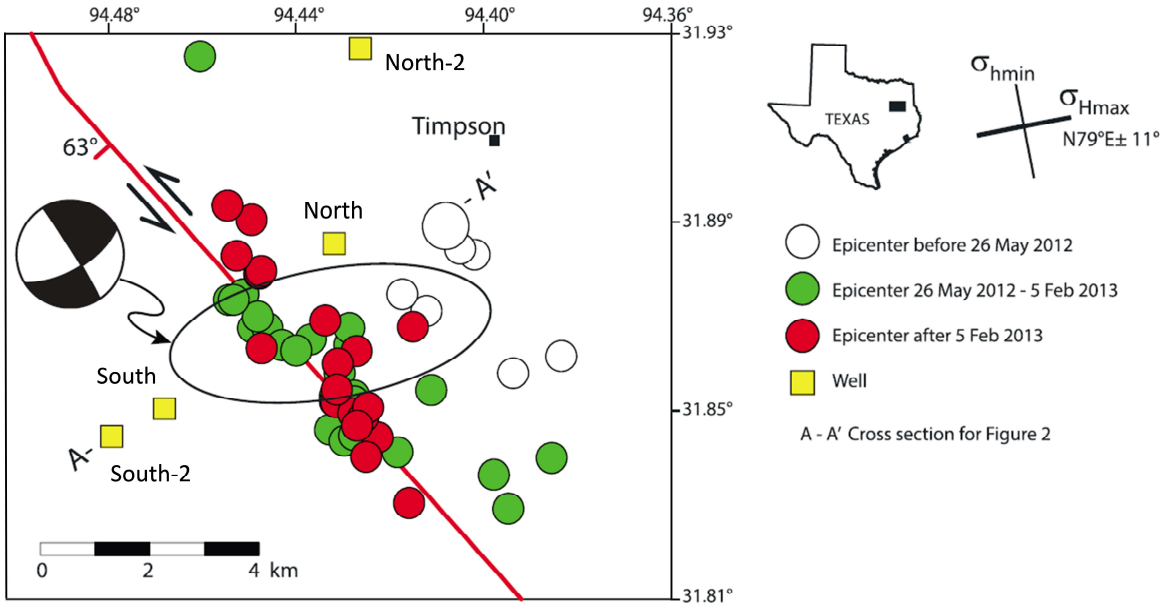

Figure 1. Map of injection wells, fault, and epicenters for the earthquake sequence near Timpson, east Texas (modified after (Fan et al. 2016; Frohlich et al. 2014)).

171 Within 5km of the highest-intensity region of the 17 May 2012 Timpson earthquake, there are two
172 high-volume and two low-volume injection disposal wells. The injection depth range of all four
173 wells is about 1.8-1.9 km, within the Rodessa of the Trinity Formation, known as an oolitic
174 sandstone (Frohlich et al. 2014). The Rodessa Formation is underlain by James Lime limestone
175 and overlain by fine crystalline anhydrite with interbedded massive anhydrite limestone and
176 dolomite. (Fan et al. 2016). In Texas, wastewater disposal activities related to petroleum
177 operations are regulated by the Texas Railroad Commission (RRC). According to the RRC's
178 database, the high-volume injection well located at the southwest of the high-intensity area, named
179 as the South well, has an averaged injection volume of 269,000 barrels (~42,700 m^3/mo) of water
180 per month (BWPM) since September 2006. The other high-volume injection well, located in the
181 north of the most affected area, has a monthly injection volume averaged 98,000 BWPM (~15,600
182 m^3/mo). As of December 2012, the total volume of injection for the North and South wells reach
183 1.05×10^6 and 2.9×10^6 m^3, respectively. Although two wells were injected with relatively high fluid
184 volume, the injection volume is within the typical range of high volume injection in Texas
185 (Frohlich et al. 2014). For the other two regional injection wells, the injection volumes were
186 considerably less. At one well, the injection took place from April 2009 to January 2010 at a rate
187 of less than 50,000 BWPM only. For the other well, injection began in March 2009 at an average
188 rate of approximately 50,000 BWPM. Due to the much lower injection volumes and further
189 distance to the epicenter, these two wells are not considered in this study.

190

3. Methodology

3.1 Model Configuration

Using the pre- and post-processor GiD (GiD 2002) and the Finite Element Modeling software DISROC (Fracsima 2016), we constructed a hydro-mechanical coupled finite element model to represent the Timpson site. Figure 2 demonstrates the connection between DISROC and GID, as well as the computational algorithm used in DISROC (see more details in section 3.2).

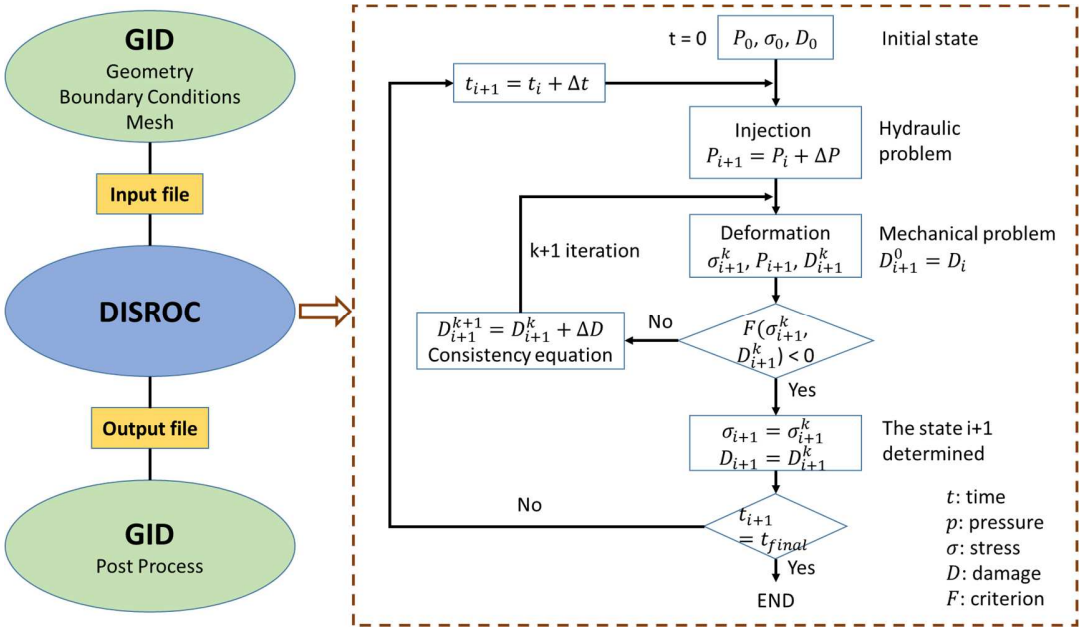

Figure 2. Overview of the integration of GID and DISROC.

Detailed information on geological settings and local stress state around the region is available in (Fan et al. 2016; Frohlich et al. 2014). Stress mapping of a broader range is available in (Snee and Zoback 2020; Snee and Zoback 2016). Two-dimensional plane strain condition was selected for higher computational efficiency. The multi-layer simulation plane is perpendicular to the fault, with both South and North injection wells indicated (Fig. 1). We adopted a similar but larger geometry as the one configured by Fan et al. (2016). The model consists of 14 layers and has a

geometry of 5 km deep by 16 km wide, with the large domain chosen to minimize both lateral and bottom boundary effects. Table 1 lists the mechanical and hydraulic parameters of each layer, including specific gravity (G_s), Young's modulus (E), shear modulus (G), Poisson's ratio (ν), porosity (n), Biot coefficient (b), permeability (K) and storage coefficient (C_{Mf}). These properties are taken following the complied data in Fan et al. (2016). According to the locations of aftershock cluster mapped by Jackson (1982), we determined the fault dip angle as 65° to the SW and imbedded it into the geometry by crossing ten layers. As shown in Figure 3, four locations were selected along the fault to study the temporal evolution of stress state under fluid injection: (1) Glen Rose layer at the top of the fault (depth of observation point = 1559 m); (2) Rodessa Aquifer where fluids were injected (highlighted in blue, with depth of observation point = 1787 m); (3) Cotton Valley formation where fault reactivation were first noticed in this study (highlighted in orange, with depth of observation point = 2785 m); and (4) Buckner formation located near the bottom of the fault (depth of observation = 3826 m). The south well is located approximately 3.75 km to the left of the fault in the Rodessa Aquifer Layer, and the North well is located 0.8 km to the right of the fault.

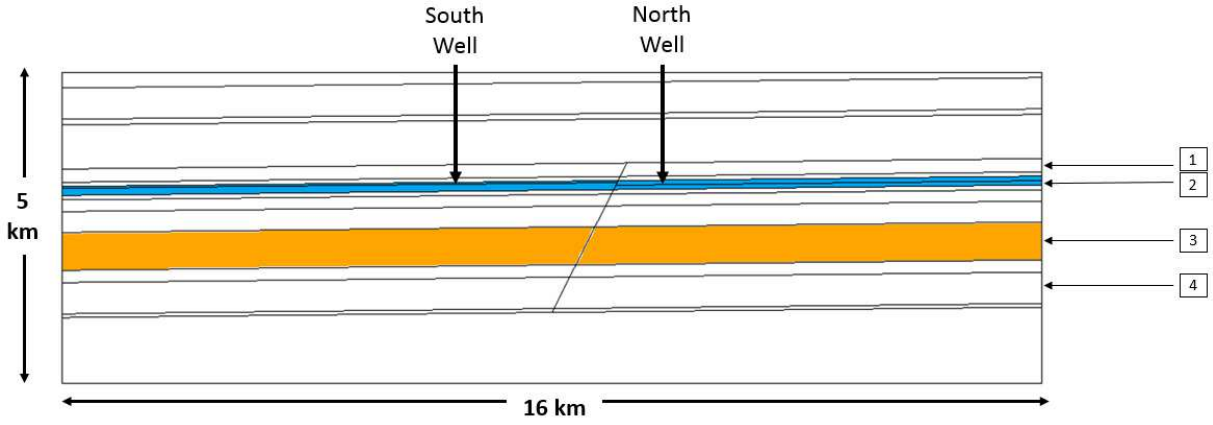

Figure 3. Finite element model geometry for the layered rock formations imbedded with a 65-degree dip angle fault (corresponding to A-A' cross section in Fig. 1). 4 locations of interest along

223 the fault are indicated by No. 1-4, located at the depths of 1559 m (Glen Rose layer), 1787 m
224 (Rodessa Aquifer), 2785 m (Cotton Valley formation), and 3826 m (Buckner formation),
225 respectively. The blue layer indicates the Rodessa Aquifer layer while the orange indicates the
226 Cotton Valley layer.

227 Based on the integration of the bulk density log of the SFE2 well calculated by Thiercelin and
228 Plumb (1994), we applied a vertical stress gradient of 24 MPa/km to the entire domain subjected
229 to gravity forces. The horizontal displacements on the left and right boundaries ($u = 0$) as well as
230 the vertical displacement on the bottom ($v = 0$) are fixed. The initial pore pressure field can be
231 obtained by imposing a hydrostatic hydraulic gradient 9.81 MPa/km to the entire domain
232 corresponding to a typical water density of 1,000 kg/m^3. In this study, for each layer, horizontal
233 stress σ_h is calculated in the model through vertical stress σ_v:

$$\sigma_h = K_0 \sigma_v \quad (1)$$

$$K_0 = \frac{\nu}{1-\nu} \quad (2)$$

234 in which K_0 is the coefficient of lateral earth pressure, and ν is Poisson's ratio.

235
236
237 Table 1. Bulk material properties of geological formations, adopted from (Fan et al. 2016).

Formation	**Starting Depth (m)**	**G_s**	**E (GPa)**	**ν (-)**	**G (GPa)**	**b (-)**	**n (%)**	**K ($\frac{m^2}{MPa*Day}$)**	**C_M ($\frac{1}{MPa}$)**
Wilcox	0	1.9	1	0.35	0.4	0.9	25	3.83E+01	1.23E-04
Midway/Navarro/Taylor Marl	244	2.6	24	0.25	10	0.9	22	2.87E+01	1.10E-04
Austin Chalk	747	2.5	18	0.25	9.6	0.95	5	9.58E-04	3.56E-05
Frederickburg Group	838	2.6	40	0.25	16	0.85	20	3.10E+01	9.84E-05
Glen Rose	1548	2.5	58	0.19	24	0.69	18	9.58E-01	8.91E-05
Massive Anhydrite	1762	2.9	57	0.2	24	0.69	10	2.87E-03	5.39E-05
Rodessa	1829	2	40	0.2	17	0.79	18	1.92E+01	9.05E-05
James Lime	1974	2.5	60	0.27	24	0.69	9	9.58E-03	4.95E-05
Pettet	2047	2.5	36	0.27	14	0.69	19	1.37E+01	9.47E-05

Travis Peak	2234	2.5	42	0.23	17	0.38	7	2.49E-03	3.63E-05
Cotton Valley	2569	2.5	62	0.13	27	0.44	8	1.44E-03	4.15E-05
Gilmer Limestone	3179	2.5	66	0.27	26	0.69	8	4.79E-02	4.51E-05
Buckner	3377	2.8	66	0.2	28	0.6	10	9.58E+00	5.26E-05
Volcanics Basement	3880	2.8	66	0.17	28	0.23	15	9.58E-01	6.93E-05

238

239 ## 3.2 Cohesive Zone Model

240 The fault instability can be modeled by constitutive models including weakening, which means
241 that the strength parameters, the cohesion and friction angle, decrease with the strain (Jaeger et al.
242 2009; Zoback 2010). A Mohr-Coulomb model of rock with friction angle decreasing with the strain
243 was used by (Rutqvist et al. 2016) to simulate induced seismicity due to fluid injection in
244 reservoirs. In this study, we considered a fault zone of finite width composed of a fault core with
245 lower permeability bounded by damage zones with higher permeability. To capture the dynamic
246 instability of fault under fluid injection activities and the degradation of both friction and cohesion,
247 we introduced a Cohesive Zone Model called "CZFrac" (model CZFrac 21510 in DISROC
248 Materials Catalog (Fracsima 2016)) for interfaces, which has the weakening property. This model
249 results from long-term researches spanning several decades in the field of Rock Mechanics,
250 especially focused on the deformation processes in rock joints and interfaces in rock-like materials
251 (Pouya and Yazdi 2015). The propagation of fractures is simulated with this model as a damage
252 process in the interface (Zhu et al. 2016), which is similar to the damage-based contact element
253 model developed by (Liao et al. 2020). The interface has, in the initial state, a cohesion which
254 decreases with the damage. At the end of this process, there remains a pure frictional contact
255 between the two faces of the interface. As the damage variable D increases from 0 (intact state) to
256 1 (completely damage state), the initial bonded interface turns into a fracture (Fig. 4).

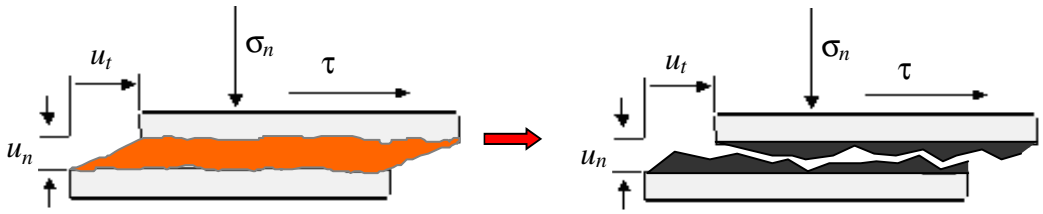

257
258 D = 0: cohesive joint D = 1: frictional contact

259 Figure 4. The damage process changes a cohesive or bonded interface to frictional contact surface.

260

261 In this study, the Cohesive Zone Model CZFrac is assigned to the interface joint element, which
262 is a four-node joint element. There is no geometrical thickness for joint elements in the numerical
263 model. To account for the fact that the fault in nature has a real physical thickness, we considered
264 the fault thickness in the material constitutive laws used for the model. The cohesive zone model
265 has both mechanical constitutive model and hydraulic properties, with its hydraulic properties
266 corresponding to a thin layer of a permeable material. Based on parametric and sensitivity analyses
267 of the model, the following properties were determined and assigned to be the same for all cohesive
268 zone elements: thickness e = 15 m (Mayolle et al. 2019), friction angle $\phi_0 = 30^o$ (Wyllie and Mah
269 2004), tensile strength $\sigma_R = 1.2$ MPa, and cohesive strength $C = 5.9$ MPa (see the equations
270 below for definition of these constants). Initial tensile and cohesive strength values used for model
271 calibration are taken within the typical ranges for rock materials (Barton 1973; Perras and
272 Diederichs 2014; Zhang 2010).

273 With fault material properties related to 10 layers of host rocks, Table 2 summarizes other
274 mechanical and hydraulic parameters for each fault segment, including normal stiffness (K_N),
275 tangential stiffness (K_T), normal permeability (C_{Nf}), tangential permeability (C_{Tf}) and storage
276 coefficient (C_{Mf}). The calculations of these properties are detailed as follows:

$$K_N = \frac{E}{e} \tag{3}$$

$$K_T = \frac{G}{e} \tag{4}$$

$$C_{Nf} = \frac{K_{core}}{e} \tag{5}$$

$$C_{Tf} = K_{core} * e \tag{6}$$

$$C_{Mf} = \left(\frac{b-n}{K_s} + \frac{n}{K_f}\right) e \tag{7}$$

277 in which K_N and K_T are obtained as the ratio between the elastic modulus of the host rock and the
278 corresponding fault thickness. The hydraulic parameters C_{Nf} and C_{Tf} represent respectively the
279 conductivity in the direction normal to the fault plane and tangent to the fault plane and are
280 obtained by assimilating the fault to a permeable layer of material with permeability K_{core} and
281 thickness e. The hydraulic storage coefficient C_{Mf} is obtained in the way from the storage
282 coefficient of the fault core material which, for a poroelastic material, is given by the inverse of its
283 Biot modulus. The Biot modulus in Eq. (7) depends on the solid grain compressibility module K_s
284 and the fluid compressibility K_f.

285

286 Table 2. Mechanical and hydraulic properties of fault segments.

Fault	**K_T (MPa/m)**	**K_N (MPa/m)**	**b_f (-)**	**C_{Tf} (m^3/MPa/day)**	**C_{Nf} (m/MPa/day)**
Glen Rose	1625	3867	0.69	4.79E+00	9.44E-04
Massive Anhydrite	1583	3800	0.69	1.44E-02	1.60E-04
Rodessa	1111	2667	0.79	4.79E+01	9.57E-04
James Lime	1575	4000	0.69	4.79E-02	3.83E-04
Pettet	945	2400	0.69	6.85E+01	9.57E-04
Travis Peak	1149	2827	0.38	1.25E-02	1.42E-04
Cotton Valley	1829	4133	0.44	7.19E-03	8.71E-05
Gilmer Limestone	1732	4400	0.69	2.40E-01	7.37E-04
Buckner	1833	4400	0.6	4.79E+01	9.57E-04
Volcanics Basement	1880	4400	0.23	4.79E+00	9.44E-04

Classical criterion such as Coulomb failure criterion is suitable for the prediction of fault reactivation (Yujie et al. 2020), but not applicable for the characterization of the subsequent instable fault slip. Instead, the cohesive zone element is governed by the strength criterion in a hyperbolic form, which is in the (σ_n, τ) plane with τ and σ_n indicating the shear and normal stresses on the interface. This type of hyperbolic shape surface results from a great number of experimental observations in Rock Mechanics and was first proposed by Lotfi and Shing (1994) and Yang and Wang (1994). This criterion is based most critically on the tensile strength, cohesion, and friction angle of the material:

$$F(\sigma, D) = \tau^2 - [h(D)\sigma_n tan\phi_0]^2 + 2h(D)g(D)\tau_c\sigma_n tan\phi_0 - g(D)^2C^2 \quad (8)$$

$$\tau_c = \frac{C^2 + \sigma_R^2 \tan^2 \phi}{2\sigma_R \tan \phi} \quad (9)$$

in which σ_n is normal stress, τ is shear stress, ϕ_0 is friction angle, and C is cohesion. σ_R is the tensile strength of the interface, and ϕ is the asymptotic friction angle. They were determined on the basis of the assumption that fault consists in a thin layer of degraded rock materials. Then σ_R, C and ϕ were chosen smaller than the lower limit of the tensile strength, cohesion and friction angle of undisturbed rock formations surrounding the fault zone. Damage variable D increases from 0 to 1, with $D = 0$ for intact state and $D = 1$ for fully fracture state. Figure 5 shows the initial strength criterion F_0 and its residual value F_r of the CZFrac model.

As shown above, the damage evolution depends on the stress applied on the material. It can be deduced from the consistency condition during the damage process. This condition expresses that the strength criterion remains constant and equal to zero during the damage process. The strength criterion surface changes in the stress plane during the damage process, but the stress must remain

on this moving surface during the damage process. As a matter of fact, the constitutive model does not allow the stress to be out of the strength domain, and if the stress is inside the strength domain there will be no more damage. The equations governing the damage D evolution are the following:

$$\dot{D} = 0 \; if \; F < 0 \tag{10}$$

$$\dot{D} = 0 \; if \; F = 0 \; and \; \frac{\partial F}{\partial \sigma}\dot{\sigma} < 0 \tag{11}$$

$$\text{If } F = 0 \; and \; \frac{\partial F}{\partial \sigma}\dot{\sigma} \geq 0, \text{ then } \dot{D} \text{ is given by } \dot{F} = \frac{\partial F}{\partial \sigma}\dot{\sigma} + \frac{\partial F}{\partial D}\dot{D} = 0 \tag{12}$$

The first equation corresponds to the stress state which has not reached the strength limit. The second equation corresponds to the unloading path from a stress state which is on the strength limit. And the third equation is related to the damage process. The equation $\dot{F} = 0$ on this line expresses the consistency condition. It allows determining the evolution of D from the stress.

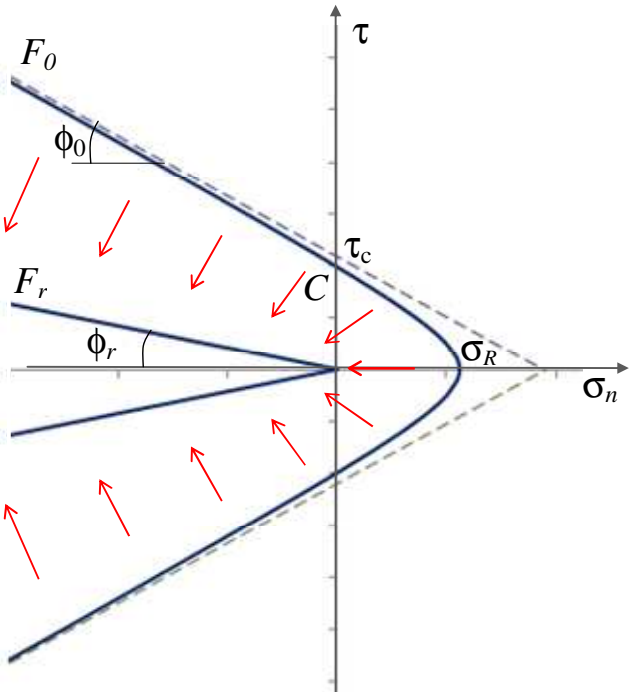

Figure 5. The strength criterion of the CZFrac model in the (σ_n, τ) plane with F_0 for the initial state and F_r for the damaged residual state.

Damage initiates when the stress state reaches the criterion representing the strength limit of the material. The evolution of these parameters is defined by two functions $g(D)$ and $h(D)$, which depend on a parameter β controlling the brittle to ductile paste of the damage process. $g(D)$ characterizes the degradation of the cohesion and tensile strength, while $h(D)$ accounts for the effect of the degradation on the friction angle.

$$g(D) = (1 - D)[1 - \beta\, ln(1 - D)] \tag{13}$$

$$h(D) = h_r + (1 - D)^{\beta'}(1 - h_r) \tag{14}$$

$$h_r = \frac{tan\phi_r}{tan\phi} \tag{15}$$

in which β and β' are ductility parameters (see DISROC Catalog of Materials (Fracsima 2016) for more details), ranging from 0 to 2, with higher values reflecting more ductile behavior of the cohesive zone element. In this study, a simplified version of this model with constant friction angle (function h remaining constant) was used for the simulations. For future studies, given the variation of friction angle upon fault slip, the model could be improved accordingly by enabling function h to incorporate that effect. The normalized shear stress versus shear displacement predicted by this model as well as its traction separation law present well a weakening behavior after a peak stress as shown in Figure 6.

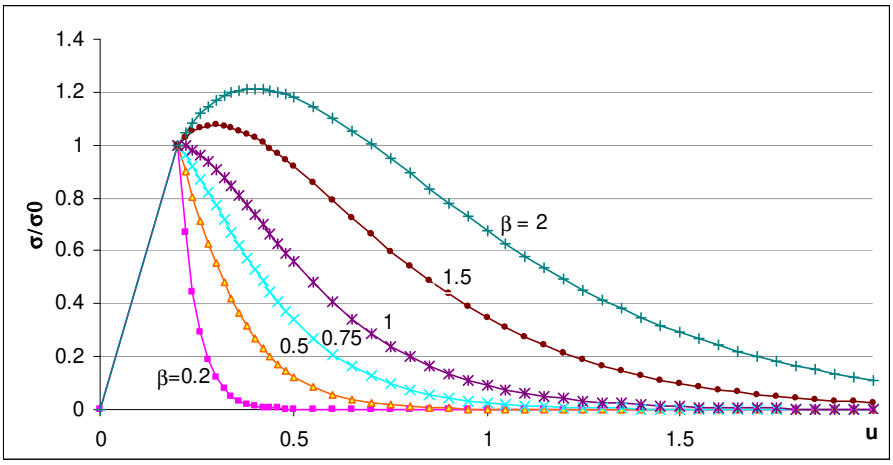

Figure 6. Traction-Separation curves for different β values. σ represents shear stress and u represents shear displacement.

This model was compared to the fracture propagation test data on a variety of rock samples and showed its capacity to represent well the fracture propagation with weakening behavior observed experimentally (Pouya and Yazdi 2015).

3.3 Injection Scenarios

In general, two typical numerical methods are available for the simulation of fluid injection, including volume-controlled and pressure-controlled conditions (Chang and Segall 2016; Fan et al. 2016). In this study, we adopted both methods to compare the effects of injection scenarios on stress perturbation and fault stability. For the volume-controlled case, as a simplified scenario, we injected fluids at a constant volume flux, obtained as an average of the pumping volumes using the field data provided by Frohlich et al. (2014) (Fig. 7). According to section 2, we took the average monthly injection rates for the South and North wells as 42,700 m^3/month and 15,600 m^3/month, respectively. In this study, the injection well geometry (i.e., the portion between ground surface and injection point) was not simulated, since this well boundary is impervious and does

not exert any hydraulic effect on the model. To better mimic the in-situ injection conditions, instead of single point injections used in prior studies (Fan et al. 2016; Zeppilli et al. 2019; Zhu et al. 2017), these fluids were injected over the perforated intervals of 15 m and 13 m within the Rodessa Aquifer layer at the South and North wells, respectively. This study did not use the one-point injection method, since the pressure at a point source is singular and so pressure control at one point is mesh-dependent. Moreover, in reality, the in-situ fluid injection usually occurs within an interval with finite length through multiple injection points. Therefore, we adopted the multiple-point fluid injection method. In the simulation, the injection rate was maintained at 93.75 m^3/day for 6 months in the South well, before the injection at the North well initiated at a constant rate of 39.47 m^3/day. Injection rates at both wells were maintained for the subsequent 7.5 years. On the other hand, pressure-controlled injection is more close to how fluids are injected in reality. Despite varying fluid volume, we maintained constant fluid pressure P throughout the duration of injection (i.e., 8 years = 96 months). This initial condition is modeled as hydrostatic state to create a uniform gradient of fluid pressure. During subsequent portions of the injection, boundaries conditions are set to have zero-flow on the lateral and bottom boundaries and P=0 is set along the top boundary of the geometry.

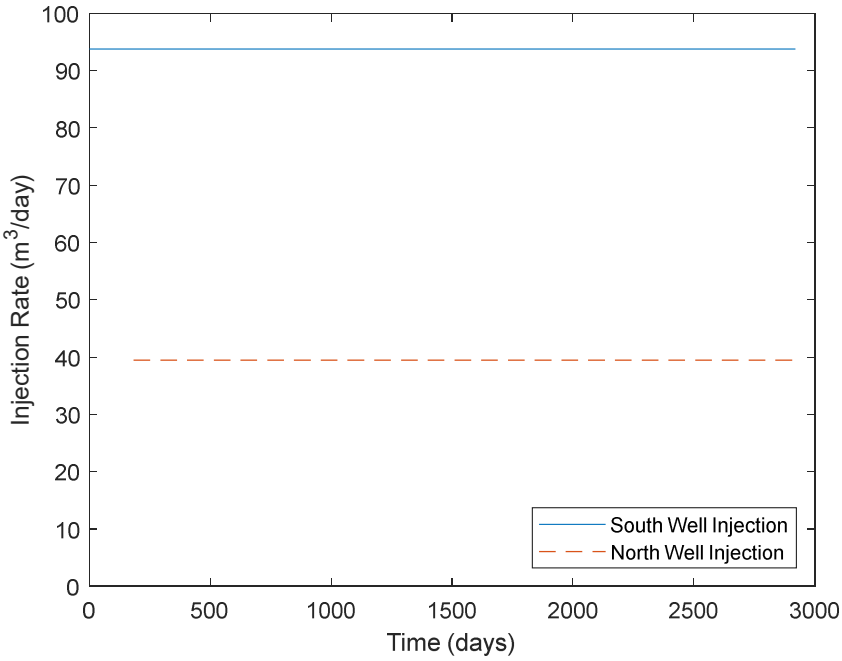

363

364 Figure 7. Simplified simulation of 8-year constant-rate fluid injection at the South and North wells
365 (for volume-controlled injection scenarios). North well injection occurred 6 months after the
366 injection through South well.

367
368

369 4. Results and Discussion

370 4.1 Initial Stress State

371 After imposing all boundary conditions and before any fluid injection activities, we calculated
372 initial stress state and pressure fields through the natural consolidation process under gravity using
373 DISROC (Fig. 8). Hydrostatic pore pressure increases linearly with depth, from 0 at ground surface
374 to 49 MPa at the bottom (Fig. 8a). Initial stresses along both horizontal and vertical directions
375 increase with depth (Figs. 8b and 8c). The initial stress state along the fault is represented by shear

and normal stress components (Fig. 8d and 8e). The general trend is that all stresses increase with depth, with similar pressure or stress obtained for the same rock layer.

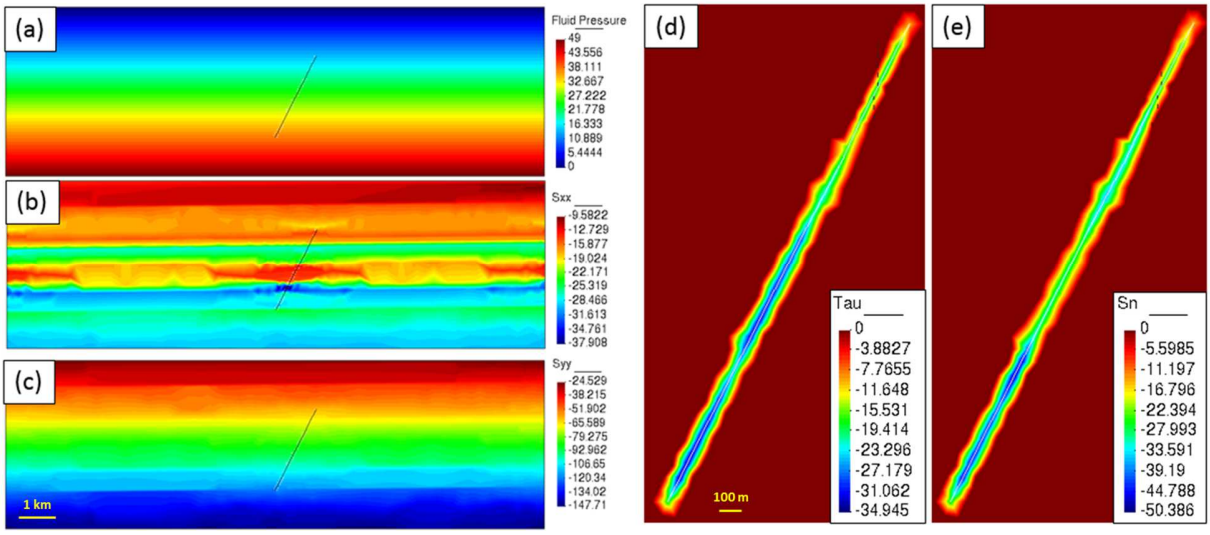

Figure 8. Initial stress states of the model after natural consolidation: (a) pore pressure; (b) horizontal stress; (c) vertical stress; (d) shear stress along the fault; and (e) normal stress along the fault. Note that all stresses are in the unit of MPa.

Figure 9 depicts the location of the initial joint stresses with respect to the initial damage criterion. Each point indicates the stress state of one joint element along the fault. All points are located within the criterion envelope, implying that the fault remains stable and no damage has occurred yet. The cluster of initial stress points circled in red are those within the Cotton Valley formation, the closest to the criterion and also the first to show signs of fault reactivations. This is also the formation with the smallest Poisson's ratio (Table 1), which explains the weaker band of horizontal stresses as seen in Figure 8b.

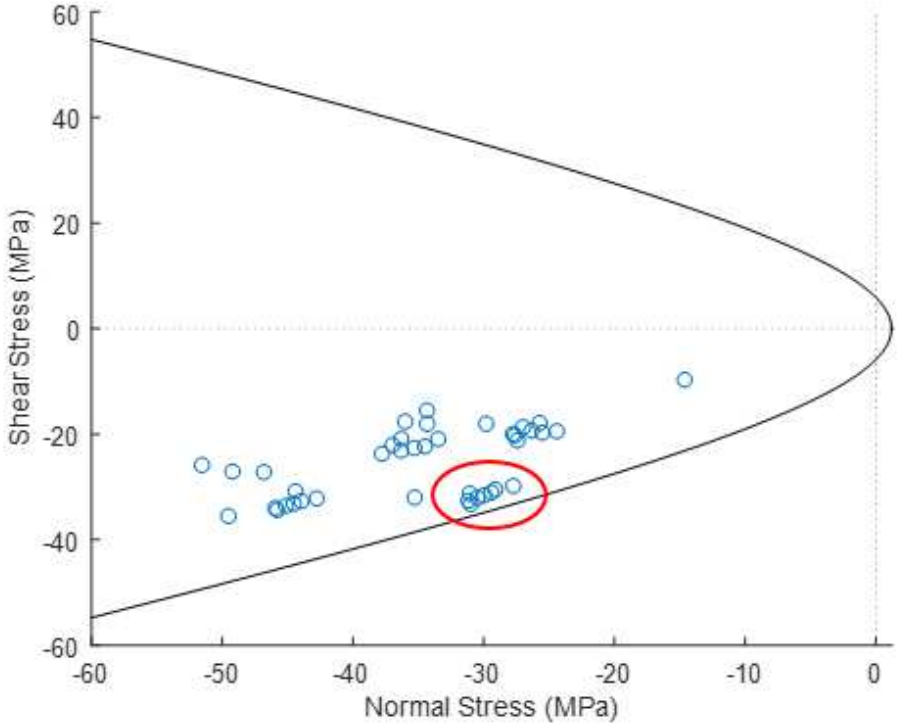

Figure 9. Initial stress state of all joint elements plotted against the damage criterion. The black curve represents the hyperbolic damage criterion. Each blue circle indicates the stress state of one joint element along the fault. The cluster of initial stress points circled in red are those within the Cotton Valley formation.

4.2 Evolution of Pore Pressure

The finite element model captures the spatiotemporal evolutions of pore pressure at the injection site during fluid injection. It should be noted that, since the exact permeability change at this specific site is unknown, this model did not consider fault-slip induced permeability changes. As described in section 2, fluid injection occurred first at the South well, with the highest pressure change observed at the injector (Fig. 10a). Note that, in comparison with single-point fluid injection adopted in prior studies (Fan et al. 2016; Zhu et al. 2017), fluids were injected through a short interval near the bottom of the injection well in this study. Fluid pressure front reached the

405 fault after just 1 day of injection. With constant injection rate at the South well, after 30-day
406 injection, the pore pressure front migrated outward from the bottom of the injection well in all
407 lateral directions (Fig. 10b). Fluid movement was primarily restricted to the injection reservoir
408 domain due to the much lower permeability of caprock and basement formations. The amount of
409 fluid injected caused a monotonic increase in pore pressures near the injection well and within the
410 reservoir layer. The fault in this case acted as a conduit, allowing fluids to flow parallel to and
411 across the fault, resulting in higher pore pressure both along and across the fault. Since tangential
412 permeability was about two orders of magnitude larger than normal permeability, pressure front
413 preferred to move along the fault, extending from the reservoir deep along the fault into the
414 basement after 6 months of injection (Fig. 10c). After this stage, injection at the North well started
415 at a lower rate, while the injection rate at the South well remained unchanged. Fluid pressure
416 changes in the subsequent 7.5 years were influenced by fluid injections from both South and North
417 wells. A significant increase of fluid pressure can be observed in the Rodessa Aquifer layer,
418 especially near the bottom of two injection wells. Since the injection rate at the South well is about
419 2.5 times higher than the rate at the North well, we observed a much higher pressure at the injector
420 of the South well (Fig. 10d). Due to the transport of fluids through the fault, fluid pressure in rock
421 formations below also increased with time.

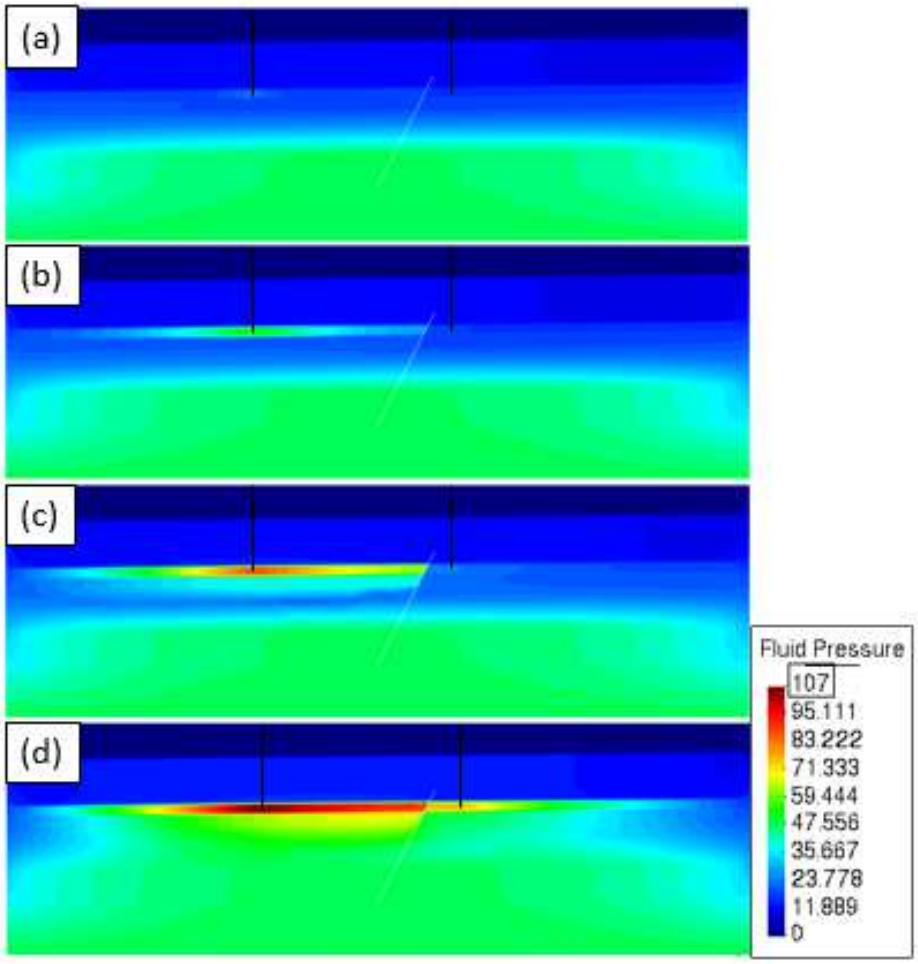

Figure 10. The distribution of fluid pressure (in MPa) after (a) 1 day, (b) 30 days, (c) 6 months, and (d) 8 years of injections.

At four observation points as mentioned in section 2, we obtained different fluid pressure evolution trends (Fig. 11). At the Rodessa Aquifer layer where fluids were injected, fluid pressure increases with the continual injection, with a transition at 120 days due to the beginning of injection at the North well. The increasing rate of fluid pressure gradually decreases with time as reflected by the curved trend. After approximately 1000 days of injection, fluid pressure at the Rodessa Aquifer layer reaches steady state, which is consistent with the findings of (Fan et al. 2016). Note that the

much higher excess pore pressure obtained at this layer may be caused by the singularity issue and numerical effect as the observation point is very close to the fracture tip. For the Glen Rose formation, because of the sealing effect of the underlying Massive Anhydrite formation, local fluid pressure only experiences a slight increase. The effect of sequential injection has minor effects on the transition of fluid pressure. Within the Buckner formation near the bottom of the fault, the fluid pressure perturbation is minimized. This sealing effect is caused by the low permeability layers (e.g., Travis Peak formation, Cotton Valley formation, and Gilmer Limestone formation) above the Buckner formation. In the Cotton Valley formation, fluid pressure is unchanged in the beginning and then increases monotonically with time. The increasing trend occurs at about 1000 days, corresponding to a similar transition time observed in the Rodessa Aquifer layer. This delayed response of fluid pressure change under injection activities is primarily contributed by the slow migration of pore pressure front and the low permeability of the Cotton Valley formation.

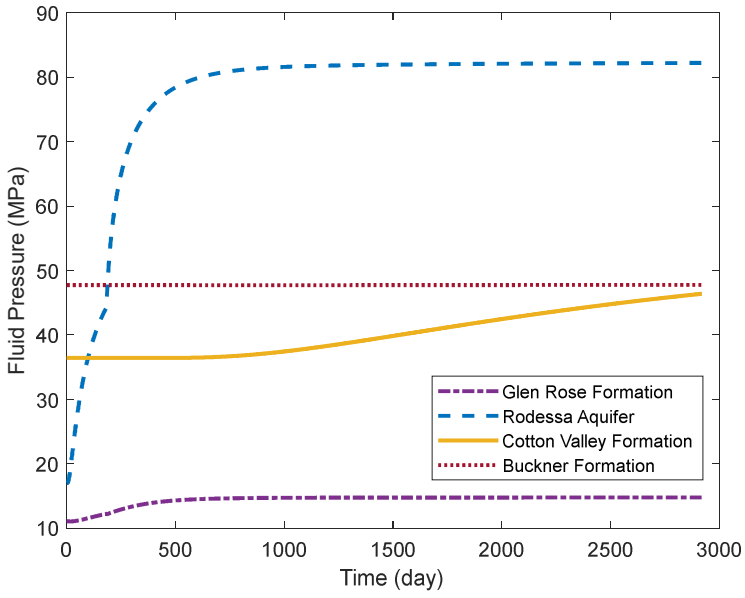

Figure 11. The temporal evolution of fluid pressure at the four layers of interest (along the fault).

4.3 Evolution of Stress Field

Due to wastewater injection activities, the geomechanical stress state of cohesive zone elements along the fault changes across different formations. Figure 12a presents the evolution of normal and shear stresses at four observation points during 8 years of fluid injections, with the enlarged view of the Glen Rose, Cotton Valley, and Buckner formations shown in Figure 11b. Since the Rodessa formation is taken for fluid disposal, it undergoes the greatest changes in both effective normal and shear stresses. The evolution of effective normal stress is directly linked to that of fluid pressure, with a clear transition visible at the moment when the North well starts its injection. In the other three formations, we observed smaller overall changes of effective normal stresses since the fluid pressure changes are limited (Fig. 12a). These gradual changes from high compression values (negative values) imply that fluid injection continously reduces the effective normal stress at the fault and increases the potential of fault reactivation, which is consistent with the findings of (Fan et al. 2016). As a result, there are two noticible sudden changes of the effective normal stress in the Cotton Valley layer, with the first occurred on day 561 (Fig. 12b for enlarged view) and the second and also the largest on day 2049 (Fig. 12b). Note that some fluctuations could be observed in the evolution curve as well, mostly originated from the nonlinear numerical computational process. In comparison to the consideration of the onset of fault reactivation in (Fan et al. 2016), simulation results obtained from this model captured the effect of fault slip on stress relexation and energy dissipation.

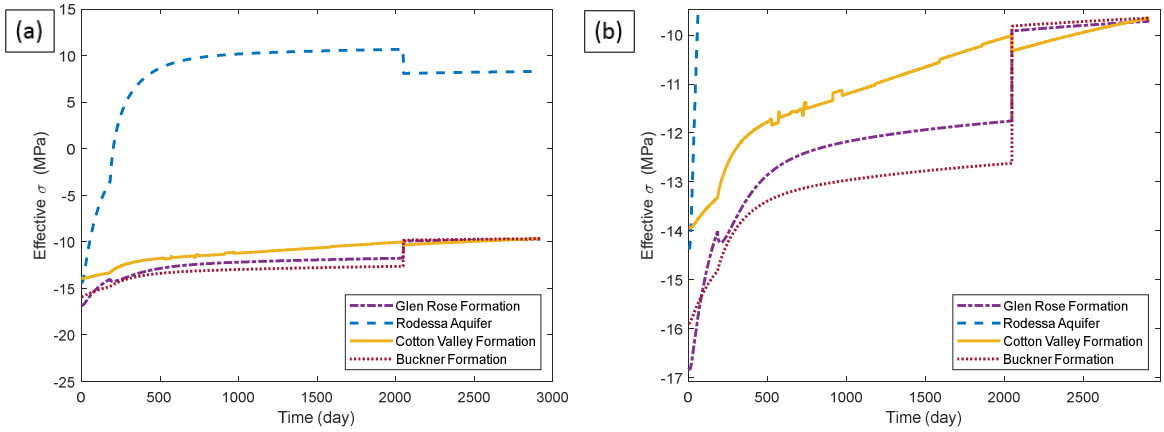

Figure 12. The evolution of effective normal stresses of four observation points (along the fault) during wastewater injection (a) for all layers and (b) zoomed in on the cotton valley formation.

Meanwhile, as shown in Figure 13a, noticible changes could be found at the same moment in the evolution of shear stresses, with the Cotton Valley and Buckner formations enlarged in Figure 13b. The shear stress values decrease slightly to -33.75 MPa on day 525 and significantly to almost 0 MPa on day 2049. These two drops correlate well with the recording of seismic activities in the field. The first event (marked by a circle) occurred after 18 months (561 days) of fluid injection and indicated the onset of seismicity. The 17 May 2012 M_w4.8 earthquake (marked by a star) occurred after about 68 months (2049 days) of fluid injection, corresponding to the duration between onset of injection and the moment when shear stress drops to zero. In comparison, previous models were able to simulate the first recorded earthquake at Timpson site (Fan et al. 2016), whereas the main shock couldn't be captured directly. It should be noted that this model did not capture the dynamic effect resulting from the main shock. It simulates the stress redistribution after failure based on the damage state in the fault, which is reasonably calculated by accounting for the failure of some cohesive zone elements and the subsequent stress update of other elements. The stress distribution obtained in this way after the failure is an equilibrium state

and does not automatically generate aftershocks, but allows to model other instabilities if the injection continues.

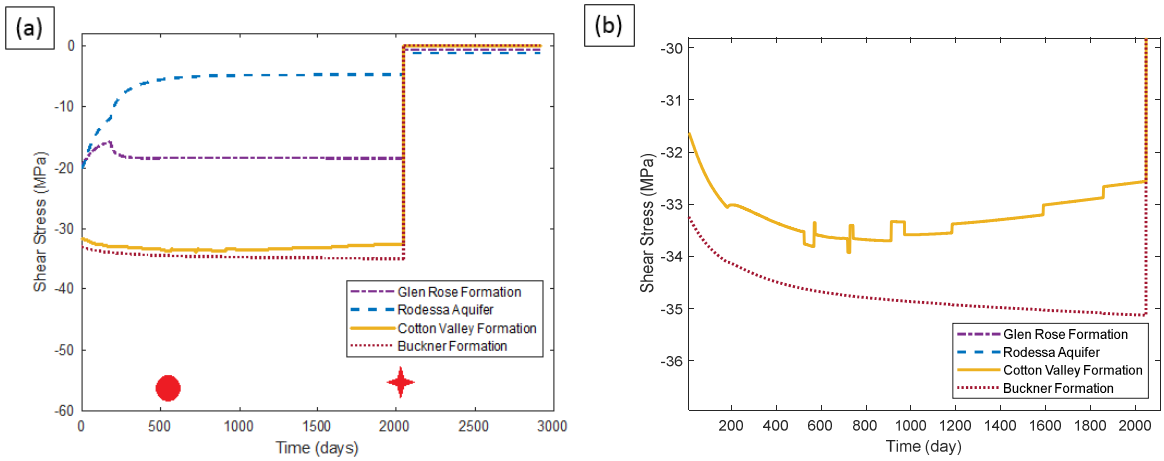

Figure 13. The evolution of shear stresses during wastewater injection (a) for all layers and (b) zoomed in on the cotton valley formation. The red circle indicates the foreshock occurred after 18 months (about 561 days) of fluid injection. The red star indicates the main shock Mw4.8 earthquake occurred after about 68 months (about 2049 days) of fluid injection.

To further depict the sudden changes of stress states along the fault, we presented the changes in horizontal stresses immediately before and after the main earthquake event that occurred on day 2049 after wastewater injection (Figure 14). Before the occurrence of the main shock, the stress field is relatively continuous across the fault. Higher stresses exist near the injection aquifer layer, which is consistent with the distribution of higher pore pressure in the same domain (Fig. 10). The domain is primarily under compression, implying the stability of the fault at that moment. Immediately after the earthquake, the stress field in this layered strata changes dramatically, especially in the vicinity of the fault (Fig. 14b). Along both sides of the fault shows a sudden

500 increase of the compressive stress, while at the fault tip shows high concentrations of tensile
501 stresses. This corresponds to the fact that the previously stable fault quickly changes its state and
502 tends to slip along opposite directions.

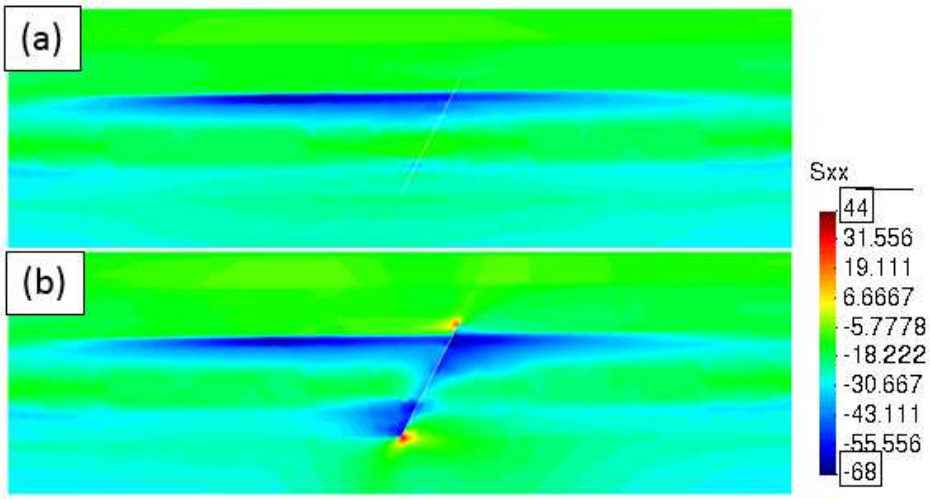

503

504 Figure 14. Sudden changes in the horizontal stresses (in MPa) immediately (a) before and (b)
505 after the damaging event occuring on day 2049 of the fluid injection.

506

507 To better understand the triggering of earthquake events, we compared the evolution of stress state
508 at four observation locations against the damage criterion (Fig. 15). The stress path of the Cotton
509 Valley formation is the only formation that intersects with the failure envelope, where other three
510 formations remain within the criterion. This indicates that, under 525 days of fluid injection,
511 damage of cohesive zone elements first initiates in the Cotton Valley formation, which is close to
512 the focal depth determined in (Frohlich et al. 2014). Poroelastic stress and pore pressure changes
513 jointly govern the fault stability. Once the criterion is met, physical properties such as cohesion,
514 tensile strength, and friction angle degrade considerably, resulting in a weaker set of parameters
515 controlling the strength criterion for this formation. The stress redistribution at the failed fault

segment induces further increase of stress on the other domains of the fault, which drives the failure of neighboring cohesive zone elements in the Buckner formation, located beneath the Cotton Valley formation. Such local instable damage propagation process triggers the more extensive damage of all cohesive zone elements along the entire fault, reflected as fault slip on day 2049.

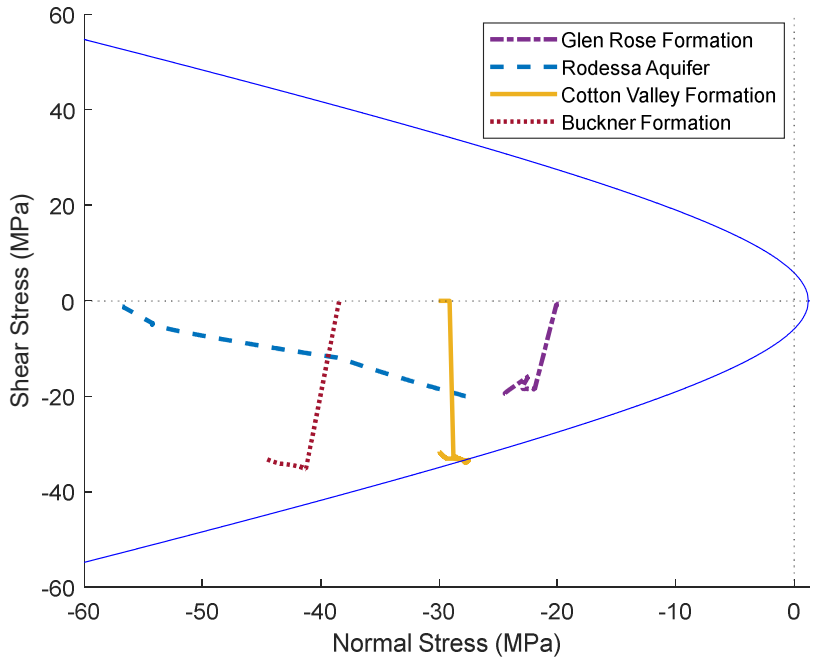

Figure 15. Damage criterion for constant flux wastewater injection over 8 years of injection. The stress path within the Cotton Valley formation exceeded the failure envelope, indicating the damage initiation reflected in cohesive zone elements.

4.4 Fault Displacement

Figure 15 compares the displacement field along the horizontal direction before and immediately after the main earthquake. The original displacement field before the onset of the main shock is continuous throughout the domain (Fig. 16a). Immediately after the onset of the main shock, we observed an instantaneous and contrasting displacement field surrounding the fault (Fig. 16b). To

530 the left of the fault shows a mixture of negative horizontal displacement along the lower part of
531 the fault and positive displacement along the upper part of the fault. Comparatively, to the right of
532 the fault shows a positive displacement field. These displacement field changes imply that the
533 breakage of fault bonding materials has occurred and led to ultimate fault slip. The progressive
534 damage of cohesive zone elements captures the effect of fault reactivation and stress redistribution
535 on the subsequent fault slip.

536

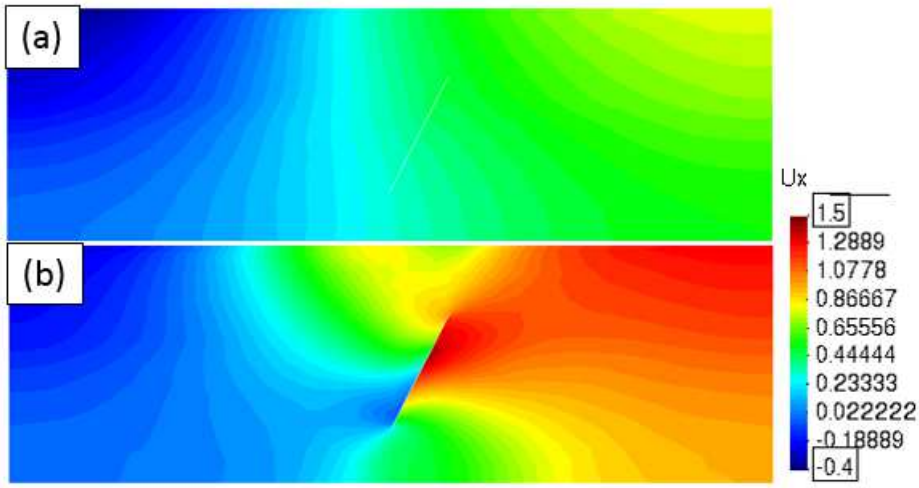

537

538 Figure 16. Sudden changes in the horizontal displacement (unit: m) immediately (a) before and
539 (b) after the damaging event occuring on day 2049 of the fluid injection.

540

541 To further investigate the process of fault reactivation and slip, we tracked the displacements of
542 cohesive zone elements at four observations points along the fault (Fig. 17). Both fault closing and
543 slip distances at all four locations are limited prior to the onset of the main shock on day 2049,
544 with the largest change obtained at the Rodessa Aquifer layer where fluids were injected. Despite
545 of the small values, slip distance changes at these points along the fault (Fig. 17c) suggests that

546 fault slip has been initiated before the main shock. On day 2049, the main shock caused a sudden
547 change in fault closing and slip distances. The main event corresponds to a sudden closing of the
548 fault at different layers, with the most significant closure of approximately 0.013 m obtained in
549 the Buckner formation. In the meantime, four locations present different slip distances, ranging
550 from 0.7 m in the Glen Rose formation to 2.4 m in the Cotton Valley formation.

551

552

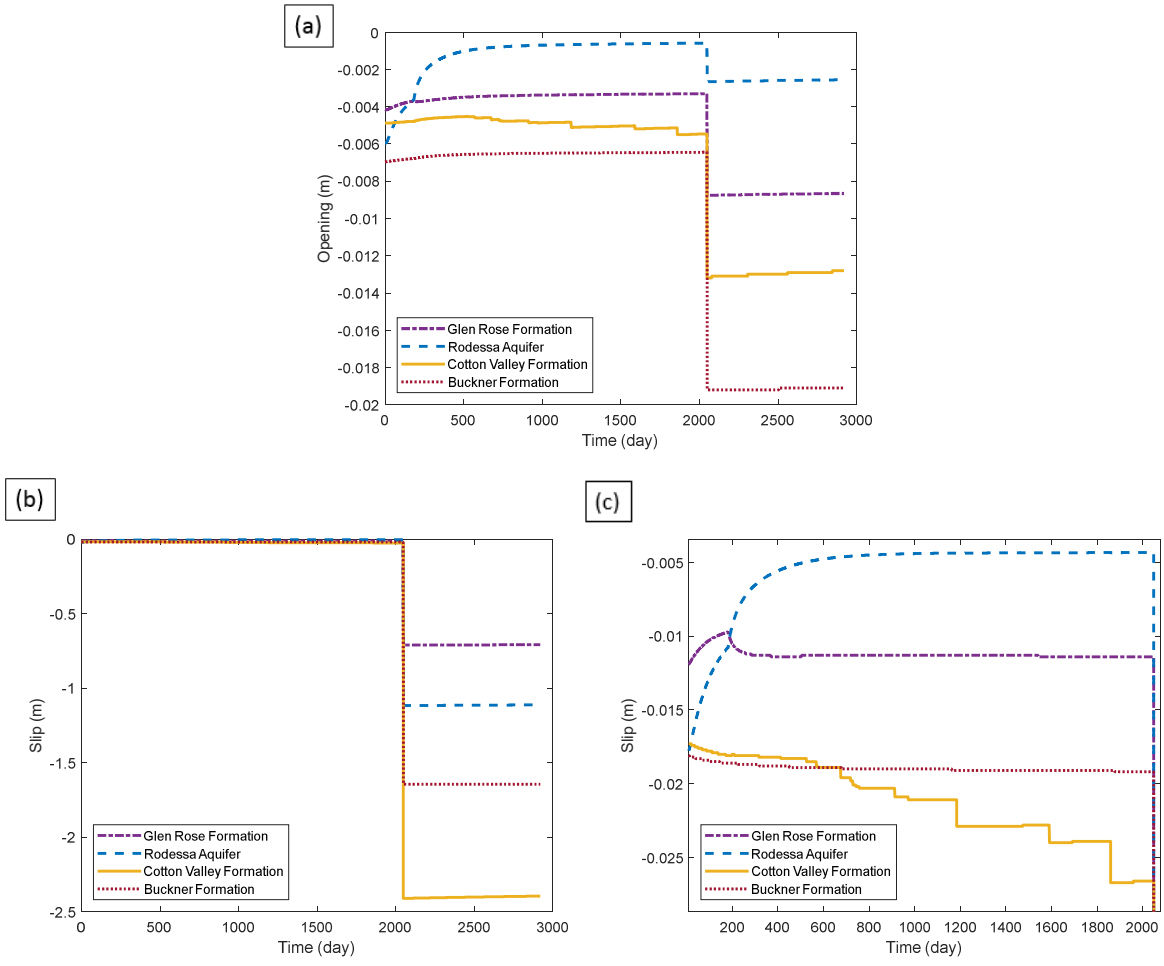

553

554 Figure 17. (a) Fault opening and (b) Fault slip during wastewater injection, with (c) a zoomed in
555 section to better view the movements of the fault before the damaging event occuring on day
556 2049 of the fluid injection.

4.5 Simulation of Pressure-Controlled Injection

While the real-life injected volumes decreased over time, the injection pressure at the surface of the injection well remained relatively constant, with an average injection pressure of 11.7 MPa at the South well and 13.6 MPa at the North well. We injected fluids under these pressures at the same injection points as those in the constant flux simulations. In this scenario, fluid pressures along the fault increased with injection and were comparable with previous studies (Fan et al. 2016; Frohlich et al. 2014). The evolution of stress state along the fault and within the Cotton Valley formation shares similar trends as those obtained from the volume-controlled scenario. The maximum change in effective normal stress was found to be 2 MPa in the Rodessa Aquifer layer, and there was a change in shear stress of 0.25 MPa. Although these stress changes were small in magnitude and did not trigger major damage, the increasing trend within 8 years of injection implies that it is still possible to exceed the damage criterion and initiate fault reactivation given sufficient injection.

After 8 years of injection, there is a maximum movement in the fault opening of 4 mm in the Rodessa Aquifer and a maximum of 0.3 mm displacement of fault slip. During the injection of wastewater under controlled pressure, the displacement of the fault was in the range of millimeters rather than the meters experienced in volume-controlled simulations, with the largest deformations observed in the Rodessa Aquifer layer and the Glen Rose formation at the top of the fault. Despite small values of fault opening during the injection, there were still be a reduction of effective normal and shear stresses of the fault. The evolution of fluid pressure under the injection of the constant pressures is shown in Figure 18. Excess pore pressure increased slightly under constant pressure injections, with the highest increase observed in the Rodessa Aquifer formation and the lowest

increase observed in the Buckner formation. This general trend is consistent with the simulation results obtained in volume-controlled injection scenarios.

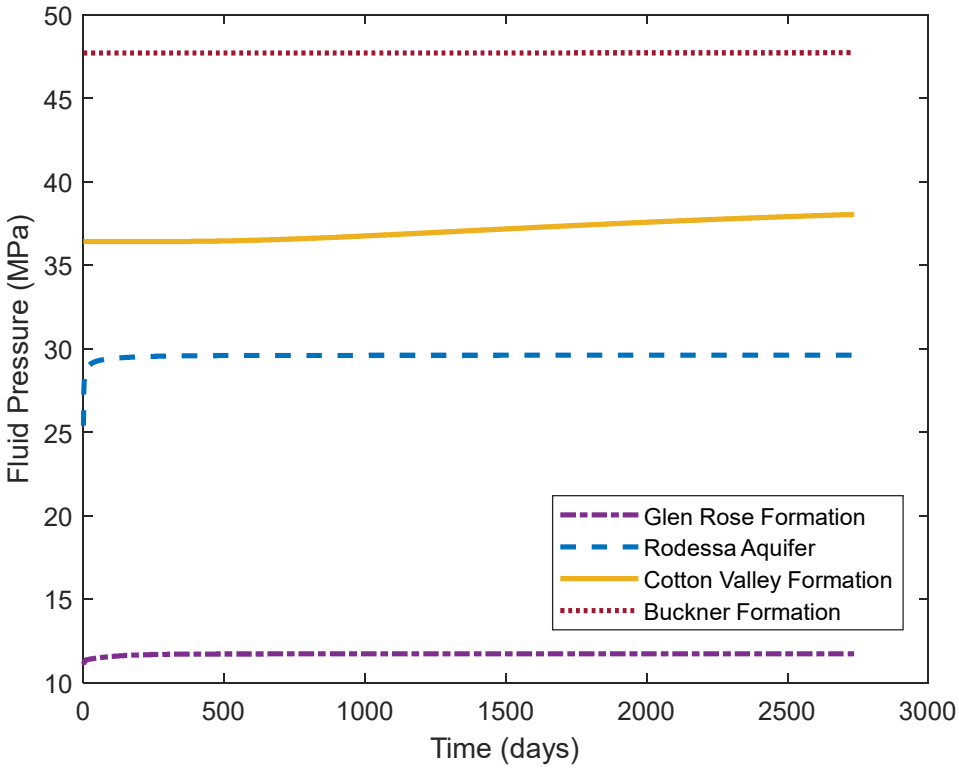

Figure 18. Fluid pressure evolution at four layers of interest along the fault under pressure-controlled fluid injection.

We think that the pressure controlled injection method needs more theoretical investigation to represent the real fluid quantities injected in the formation. In general, the integration of velocity around the borehole circumference gives the injection rate:

$$q = \oint v_r ds = \oint -k\partial_r p ds \tag{11}$$

591 in which p is the pressure, $\partial_r p$ is the pressure gradient in the radial direction, k is the permeability,
592 v_r is the radial fluid velocity, and s is the curvilinear abscissa on the circumference. If we assume
593 that the borehole diameter is small compared to the whole domain, for a given pressure, the
594 variation of its diameter changes only slightly the pressure gradient. But the injection rate, given
595 by the circumference integral, is proportional to the borehole diameter. Therefore, it is reasonable
596 to state that injection volume is dependent on the borehole diameter. In the above simulations, the
597 pressure is imposed on a point representing the borehole location, but the borehole diameter is not
598 geometrically taken into account. This explains that smaller fluid volumes are injected in the
599 formation and so smaller effects are obtained. This problem would not happen in a 3D modeling
600 where the borehole diameter could be explicitly introduced in the model. We think that, for 2D
601 modeling of fluid injection by pressure control at the at the borehole bottom, more theoretical
602 investigation is needed to determine the adequate or equivalent pressure to be imposed.

603

604 **5 Conclusions**

605 To investigate the geomechanical correlation between fluid injection activities and fault instability
606 in Timpson, Texas, we simulated the hydro-mechanical coupled processes of pore pressure and
607 stress changes and their effects on fault reactivation and slip. A finite element model enriched with
608 cohesive zone elements was built based on the geological, in-situ stress, and operational conditions
609 summarized in published data. Simulation results reflect the spatiotemporal evolution of pore
610 pressure and stress field in the layered formations and lead to the following major conclusions:

611 (1) With the continual fluid injection, pore pressure increases and gradually stabilizes, which is
612 more evident in regions close to the injection layer. Pore pressure perturbation in a certain layer

depends on injection duration and rate, as well as the permeability of overlying and underlying formations. At Timpson site, a significant increase of pore pressure can be observed in the Rodessa Aquifer layer, especially near the bottom of two injection wells.

(2) The evolution of effective stress is directly linked to pore pressure, with the largest change observed in the Rodessa Aquifer layer where fluids are injected. Fluid injection continously reduces the effective normal stress along the fault and increases the potential of fault reactivation. The triggering of fault instability is associated with sudden stress relaxations, with the first drop occurred on day 561 and the largest drop on day 2049 after the onset of fluid injection. This matches reasonably well with the time history of the foreshock and main shock events recorded during the 2012 Timpson earthquake sequence.

(3) Changes in the displacement field imply that the breakage of fault bonding materials has occurred and led to the ultimate fault slip. The progressive damage of cohesive zone elements captures the effect of fault reactivation and stress redistribution on the subsequent fault slip and energy dissipation. The main event corresponds to a sudden closing of the fault at different layers, with the most significant closure of approximately 0.013m obtained in the Buckner formation and the largest slip distance 2.4m in the Cotton Valley formation.

(4) The evolution of stress state along the fault and within the Cotton Valley formation from pressure-controlled scenario shares similar trends as those obtained from the volume-controlled scenario. More theoretical investigations are needed for 2D modeling of pressure-controlled fluid injection at the borehole bottom, in order to determine the adequate or equivalent pressure to be imposed.

In summary, this study shows that the seismicity induced by wastewater injection in the two studied injection wells is plausible at the Timpson site. The developed finite element model that

employs cohesive zone model to define fault zones improves assessments of the potential for both fault reactivation and later slip due to fluid injection.

Fund

This research is supported by Open Fund (PLN201801) of State Key Laboratory of Oil and Gas Reservoir Geology and Exploitation (Southwest Petroleum University). The Chateaubriand Fellowship offered by the Embassy of France in the United States is also greatly appreciated.

Compliance with ethical standards

Conflict of interest

The authors declare that they have no conflict of interest.

References

Barbour AJ, Norbeck JH, Rubinstein JL (2017) The effects of varying injection rates in Osage County, Oklahoma, on the 2016 M w 5.8 Pawnee earthquake Seismological Research Letters 88:1040-1053

Barton N (1973) Review of a new shear-strength criterion for rock joints Engineering geology 7:287-332

Block LV, Wood CK, Yeck WL, King VM (2014) The 24 January 2013 ML 4.4 earthquake near Paradox, Colorado, and its relation to deep well injection Seismological Research Letters 85:609-624

Chang K, Segall P (2016) Injection-induced seismicity on basement faults including poroelastic stressing Journal of Geophysical Research: Solid Earth 121:2708-2726

Chen G-J (2003) Analysis of pumping in multilayered and poroelastic half space Computers and Geotechnics 30:1-26

Cheng A-D, Detournay E (1998) On singular integral equations and fundamental solutions of poroelasticity International Journal of Solids and Structures 35:4521-4555

Da Silva BG, Einstein HH (2013) Modeling of crack initiation, propagation and coalescence in rocks International journal of fracture 182:167-186

Detournay E, Cheng AH (1987) Poroelastic solution of a plane strain point displacement discontinuity

Ellsworth WL (2013) Injection-induced earthquakes Science 341:1225942

Fan Z, Eichhubl P, Gale JF (2016) Geomechanical analysis of fluid injection and seismic fault slip for the Mw4. 8 Timpson, Texas, earthquake sequence Journal of Geophysical Research: Solid Earth 121:2798-2812

Fan Z, Eichhubl P, Newell P (2019) Basement fault reactivation by fluid injection into sedimentary reservoirs: Poroelastic effects Journal of Geophysical Research: Solid Earth 124:7354-7369

Fracsima (2016) DISROC, a Finite Element Code for modelling Thermo-Hydro-Mechanical processes in fractures porous media (http://www.fracsima.com/DISROC).
Frohlich C (2012) Two-year survey comparing earthquake activity and injection-well locations in the Barnett Shale, Texas Proceedings of the National Academy of Sciences 109:13934-13938
Frohlich C, Davis SD (2002) Texas earthquakes vol 2. University of Texas Press,
Frohlich C, DeShon H, Stump B, Hayward C, Hornbach M, Walter JI (2016) A historical review of induced earthquakes in Texas Seismological Research Letters 87:1022-1038
Frohlich C, Ellsworth W, Brown WA, Brunt M, Luetgert J, MacDonald T, Walter S (2014) The 17 May 2012 M4. 8 earthquake near Timpson, East Texas: An event possibly triggered by fluid injection Journal of Geophysical Research: Solid Earth 119:581-593
Frohlich C, Hayward C, Stump B, Potter E (2011) The Dallas–Fort Worth earthquake sequence: October 2008 through May 2009 Bulletin of the Seismological Society of America 101:327-340
GiD (2002) The personal pre and postprocessor. International Center for Numerical Methods in Engineering (CIMNE), URL: www.gidhome.com.
Gunarathna G, da Silva BG (2019) Influence of the effective vertical stresses on hydraulic fracture initiation pressures in shale and engineered geothermal systems explorations Rock Mechanics and Rock Engineering 52:4835-4853
Haddad M, Eichhubl P (2020) Poroelastic models for fault reactivation in response to concurrent injection and production in stacked reservoirs Geomechanics for Energy and the Environment:100181
Healy J, Rubey W, Griggs D, Raleigh C (1968) The denver earthquakes Science 161:1301-1310
Hornbach MJ et al. (2015) Causal factors for seismicity near Azle, Texas Nature communications 6:6728
Horton S (2012) Disposal of hydrofracking waste fluid by injection into subsurface aquifers triggers earthquake swarm in central Arkansas with potential for damaging earthquake Seismological Research Letters 83:250-260
Hsieh PA, Bredehoeft JD (1981) A reservoir analysis of the Denver earthquakes: A case of induced seismicity Journal of Geophysical Research: Solid Earth 86:903-920
Jackson MPA (1982) Fault Tectonics of the East Texas Basin vol 82. Bureau of Economic Geology, The University of Texas at Austin
Austin, Texas
Jaeger JC, Cook NG, Zimmerman R (2009) Fundamentals of rock mechanics. John Wiley & Sons,
Johann L, Shapiro SA, Dinske C (2018) The surge of earthquakes in Central Oklahoma has features of reservoir-induced seismicity Scientific reports 8:1-14
Kang J-Q, Zhu J-B, Zhao J (2019) A review of mechanisms of induced earthquakes: from a view of rock mechanics Geomechanics and Geophysics for Geo-Energy and Geo-Resources 5:171-196
Keranen KM, Weingarten M, Abers GA, Bekins BA, Ge S (2014) Sharp increase in central Oklahoma seismicity since 2008 induced by massive wastewater injection Science 345:448-451
Kim WY (2013) Induced seismicity associated with fluid injection into a deep well in Youngstown, Ohio Journal of Geophysical Research: Solid Earth 118:3506-3518
Lei Q, Doonechaly NG, Tsang C-F (2021) Modelling fluid injection-induced fracture activation, damage growth, seismicity occurrence and connectivity change in naturally fractured rocks International Journal of Rock Mechanics and Mining Sciences 138:104598
Liao Z, Ren M, Tang C, Zhu J (2020) A three-dimensional damage-based contact element model for simulating the interfacial behaviors of rocks and its validation and applications Geomechanics and Geophysics for Geo-Energy and Geo-Resources 6:1-21
Lotfi HR, Shing PB (1994) Interface model applied to fracture of masonry structures Journal of structural engineering 120:63-80
Mayolle S, Soliva R, Caniven Y, Wibberley C, Ballas G, Milesi G, Dominguez S (2019) Scaling of fault damage zones in carbonate rocks Journal of Structural Geology 124:35-50
McGarr A (2014) Maximum magnitude earthquakes induced by fluid injection Journal of Geophysical Research: solid earth 119:1008-1019
McGarr A et al. (2015) Coping with earthquakes induced by fluid injection Science 347:830-831
Perras MA, Diederichs MS (2014) A review of the tensile strength of rock: concepts and testing Geotechnical and geological engineering 32:525-546
Pouya A, Yazdi PB (2015) A damage-plasticity model for cohesive fractures International Journal of Rock Mechanics and Mining Sciences 73:194-202

Rajapakse R, Senjuntichai T (1993) Fundamental solutions for a poroelastic half-space with compressible constituents
Rubinstein JL, Mahani AB (2015) Myths and facts on wastewater injection, hydraulic fracturing, enhanced oil recovery, and induced seismicity Seismological Research Letters 86:1060-1067
Rudnicki JW (1986) Fluid mass sources and point forces in linear elastic diffusive solids Mechanics of Materials 5:383-393
Rutqvist J et al. (2016) Fault activation and induced seismicity in geological carbon storage–Lessons learned from recent modeling studies Journal of Rock Mechanics and Geotechnical Engineering 8:789-804
Rutqvist J, Rinaldi AP, Cappa F, Moridis GJ (2013) Modeling of fault reactivation and induced seismicity during hydraulic fracturing of shale-gas reservoirs Journal of Petroleum Science and Engineering 107:31-44
Segall P, Lu S (2015) Injection-induced seismicity: Poroelastic and earthquake nucleation effects Journal of Geophysical Research: Solid Earth 120:5082-5103
Selvadurai A, Kim J (2015) Ground subsidence due to uniform fluid extraction over a circular region within an aquifer Advances in Water Resources 78:50-59
Shirzaei M, Ellsworth WL, Tiampo KF, González PJ, Manga M (2016) Surface uplift and time-dependent seismic hazard due to fluid injection in eastern Texas Science 353:1416-1419
Shirzaei M, Manga M, Zhai G (2019) Hydraulic properties of injection formations constrained by surface deformation Earth and Planetary Science Letters 515:125-134
Snee J-EL (2020) State of Stress in North America: Seismicity, Tectonics, and Unconventional Energy Development. Stanford University,
Snee J-EL, Zoback MD (2020) Multiscale variations of the crustal stress field throughout North America Nature Communications 11:1-9
Snee JEL, Zoback MD (2016) State of stress in Texas: Implications for induced seismicity Geophysical Research Letters 43:10,208-210,214
Thiercelin M, Plumb R (1994) A core-based prediction of lithologic stress contrasts in east Texas formations SPE Formation Evaluation 9:251-258
Walsh III FR, Zoback MD (2016) Probabilistic assessment of potential fault slip related to injection-induced earthquakes: Application to north-central Oklahoma, USA Geology 44:991-994
Wang K, Ellsworth W, Beroza GC (2020) Revisiting the Timpson Induced Earthquake Sequence: A System of Two Parallel Faults Geophysical Research Letters 47:e2020GL089192
Wang R, Kümpel H-J (2003) Poroelasticity: Efficient modeling of strongly coupled, slow deformation processes in a multilayered half-space Geophysics 68:705-717
Weingarten M, Ge S, Godt JW, Bekins BA, Rubinstein JL (2015) High-rate injection is associated with the increase in US mid-continent seismicity Science 348:1336-1340
Wyllie DC, Mah C (2004) Rock slope engineering. CRC Press,
Yang H, Wang ML (1994) Constitutive theory of interface behavior in quasi-brittle materials Journal of engineering mechanics 120:2588-2603
Yeo I, Brown M, Ge S, Lee K (2020) Causal mechanism of injection-induced earthquakes through the M w 5.5 Pohang earthquake case study Nature communications 11:1-12
Yujie Z, Xiaoli L, Enzhi W (2020) Influence of impoundment gravity and pore pressure on reactivation of faults Geomechanics and Geophysics for Geo-Energy and Geo-Resources 6:1-19
Zeppilli D, Zhu C, Pouya A Joint-enriched Finite Element Modeling of Fault Slip under Fluid Injection in Reservoir Faults. In: 53rd US Rock Mechanics/Geomechanics Symposium, 2019. American Rock Mechanics Association,
Zhai G, Shirzaei M (2018) Fluid injection and time-dependent seismic hazard in the Barnett Shale, Texas Geophysical Research Letters 45:4743-4753
Zhang L (2010) Estimating the strength of jointed rock masses Rock mechanics and rock engineering 43:391-402
Zhu C, Fan Z, Eichhubl P The effect of variable fluid injection rate on the stability of seismogenic faults. In: 51st US Rock Mechanics/Geomechanics Symposium, 2017. American Rock Mechanics Association,
Zhu C, Pouya A, Arson C (2016) Prediction of viscous cracking and cyclic fatigue of salt polycrystals using a joint-enriched finite element model Mechanics of Materials 103:28-43
Zoback MD (2010) Reservoir geomechanics. Cambridge University Press,